A Combinational NMR and Dielectric Technique Using Spectral NMR Mapped Distributions of Dielectric Relaxation

James Funk[1,*], *Michael* Myers[1], and *Lori* Hathon[1]

[1]University of Houston, Department of Petroleum Engineering, 5000 Gulf Freeway, Houston, Texas, 7723

Abstract. Combinations of NMR and dielectric measurements frequently address challenging saturation determinations and wettability in conventional reservoirs. When pore structure effects are addressed, the NMR characteristics are well documented. However, the dielectric measurement response is attributed to the "texture" of the rock matrix. This simple pore structure descriptor can be improved if the electromagnetic constitutive equations and the governing physics in both measurements are considered. Similar to the dipolar relaxation equivalence of NMR and dielectric correlation time measurements in the BPP model, we develop a relaxation time correlation assuming representative Maxwell-Wagner relaxations. The key carbonate pore components demonstrated by Myers are used along with diffusion measurements and analyses to relate the Maxwell-Wagner effect to the Brownstein and Tarr model for surface relaxivity. The distributions of dielectric relaxation times in carbonate dispersion curves from 1 – 300 MHz are quantified using the Havriliak-Negami (HN) model. The quantifications are used to evaluate characteristic dielectric dispersions curves from a dielectric carbonate model with multiple pore systems. The modeled pore system fractions are spectrally mapped to the NMR T_1 or T_2 distributions based on enhanced Debye shielding distances correlated with the conductivity. The characterized NMR distributions provide additional petrophysical insight for the frequently used Archie exponent combination (MN) associated with the water tortuosity.

1 Introduction

One of the fundamental ideas expressed in the classic paper by Bloembergen, Purcell, and Pound [1] focused on using molecular autocorrelation functions to compare dielectric and nuclear magnetic resonance (NMR) relaxation. In their quantification of "the effect of the thermal motion of the magnetic nuclei upon spin-spin interaction" they observe;

> *Values of tc for ice, inferred from nuclear relaxation measurements, correlate well with dielectric dispersion data.*

Applications of this comparative approach have been used extensively in polymer chemistry [2] and in bio-molecular protein conformational studies [3] [4]. Recent dielectric and NMR comparative approaches in the macromolecular chemistry field have incorporated the technique of fast-filed cycling NMR that looks at dispersion in a magnetic field [5].

The exclusive use of the individual NMR and dielectric techniques for critical petrophysical parameters such as saturation, wettability, and pore morphology has been successful and well documented. The optimal combination techniques have been in the lower frequency range (spectral induced polarization, (SIP)[6, 7] and the low-frequency limit[8], where combinations of Archie's law conductivity and NMR surface relaxivity dominate.

Combinational use of dielectric and NMR measurements in petrophysics usually considers the two techniques as distinct processes that provide selective choices for different petrophysical parameter such as porosity or "water tortuosity". Comparisons of derived parameters and mechanisms of the two tools are infrequent except in the evaluation of wettability[9-11].

Our focus on the combinations of dielectric and NMR tests employs a basic distributional model to address petrophysical characterizations using relaxation dynamics that emphasize the pore and water structure interactions [12, 13].

In this comparative approach we map dielectric dispersion time constants onto an NMR distributional structure. We use NMR measurements at 2 MHz and 23 MHz, along with dielectric measurements in the frequency range dominated by the Maxwell-Wagner effect. Results of the experiments are modeled with a hybrid relaxation-effective medium model, validated with petrophysical imaging techniques, and correlated with existing saturation and diffusion models.

* Corresponding author: manager.coreimaging@gmail.com

1.1 Autocorrelation and Molecular Motion Induced Relaxation Mechanisms

A typical dielectric dispersion experiment relies on the establishment of a frequency varied electric field, whose Fourier transform provides a distribution of molecular motion-induced time decay constants reflecting electromagnetic (EM) polarization. A typical NMR experiment also shows a molecular motion-induced decay, in this case decay of EM magnetization.

Although characterized decay constants between the two phenomena are orders of magnitude different, they are both tied intimately to the autocorrelation time for molecular motion (protons in NMR, bound dipoles in Debye water relaxation, hydrated ions in Maxwell-Wagner relaxation). Confusingly, in NMR where T_1 times are in seconds, the dielectric time constant is in pico-seconds. As Callaghan [14] mentioned:

> *Nothing quite so baffles the general physics community as the idea of motional averaging and its consequence of slow NMR signal decays arising from fast motion.*

The mathematical models that describe and incorporate motional averaging time constants in NMR T_1 and T_2 values or dielectric τ_C are described in following sections.

1.1.1 NMR

In the Bloembergen, Purcell, and Pound paper the quantitative characterization of NMR relaxation in terms of autocorrelation time constants gives:

$$\frac{1}{T_1} = K\left[\frac{\tau_c}{1+\omega_0^{\,2}\tau_c^{\,2}} + \frac{4\tau_c}{1+4\omega_0^{\,2}\tau_c^{\,2}}\right] \quad (1)$$

$$\frac{1}{T_2} = \frac{K}{2}\left[3\tau_c + \frac{5\tau_c}{1+\omega_0^{\,2}\tau_c^{\,2}} + \frac{2\tau_c}{1+4\omega_0^{\,2}\tau_c^{\,2}}\right] \quad (2)$$

Where the constant K is , $K = \frac{3\mu_0^{\,2}}{160\pi^2}\cdot\frac{\hbar^2\gamma^4}{r^6}$

Each term is characteristic of a particular frequency dependent, polarization direction, molecular motion induced relaxation. Relaxation rate variations with autocorrelation time are illustrated in Figure 1 for higher and lower fields exemplified with our 2 and 23 MHz systems.

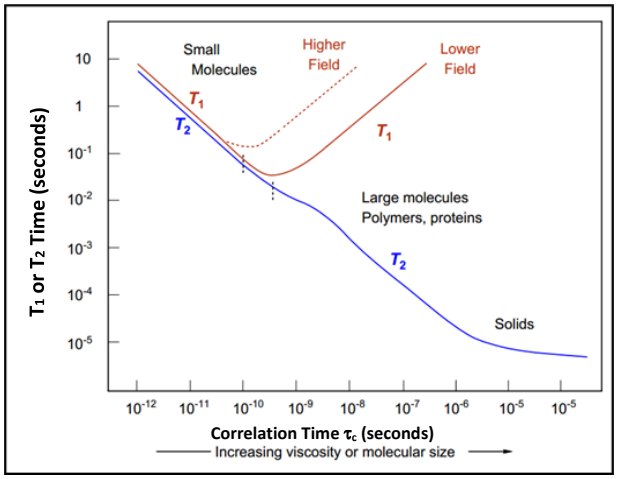

Figure 1 - Plot of the BPP model calculations showing the T_1 and T_2 response and departures from the "line narrowing" range (T_1=T_2) as a function of autocorrelation time τ_c.

1.1.2 Dielectrics

Similar to the additive relaxation (magnetization) mechanisms in NMR, dielectric processes can be described by their fundamental polarization mechanisms. Total polarization in the frequency range of this study can be characterized by three components correlated with the rock matrix, the fluids in the system, and the interface between the matrix and the fluids.

1.1.3 Rock Matrix - Electronic and Ionic Polarization - High-Frequency Limit

Distortion of the electron cloud around an atom and its return to equilibrium is a short, fast process extending into the electromagnetic spectrum's ultraviolet region. In crystalline materials and other solids, ionic polarization due to the relative displacement or vibrations of ionic lattice charges provides an additional relaxation mechanism extending into the EM spectrum [15]. These characteristics are the basis for the standards used in dielectric measurements and the termed “high-frequency limit” characteristics incorporated in most dielectric models.

1.1.4 Pore Fluids - Dipolar Relaxation - Water Structure

The interaction of EM energy with materials containing permanent dipoles has been a significant basis for work with dielectrics [13, 16-19]. The founding ideas are based on the original work of Debye on the dipole moment of water. Although induced dipoles in non-polar materials are significant in applied spectroscopic fields, for work with natural materials, the primary concern is with the permanent dipole moment of water. Although it is categorized differently as a bound charge effect [20], an orientational effect, or a surface effect [21], the process of dipolar orientation and relaxation describe an essential characteristic of the structure of water [12, 19].

Debye's work in 1929 resulted in an expression for the dielectric constant of water based on the relaxation time constant as,

$$\varepsilon^* = \varepsilon_\infty + \frac{(\varepsilon_s - \varepsilon_\infty)}{(1 + i\,\omega\,\tau_c)} \quad (3)$$

1.1.5 *Interfacial Polarization – Maxwell-Wagner Effect*

Restricted charge movement in complex structures adds to the dielectric storage through a structure-dependent polarization process. These complex systems exhibit non-Debye relaxation described empirically as distorted Cole-Cole plots. A frequently used representation of this and the one used in this study is the Havriliak-Negami (HN) model [22],

$$\varepsilon^* = \varepsilon_\infty + \frac{(\varepsilon_s - \varepsilon_\infty)}{(1 + (i\,\omega\,\tau_c)^\alpha)^\beta} \quad (4)$$

2 Experimental

2.1 Petrophysical Imaging and Measurement Sequence

Micro-CT images were acquired on the samples using a XTekCT micro-CT scanner operating at 110 KeV and 130 micro-amps. The flat panel detector provided an image resolution of 34.7 microns on a one-inch diameter sample. Samples were scanned in a cleaned and dried state with x-ray projections taken at 0.119-degree increments.

Image analyses were performed using Dragonfly software (Object Research Systems, Montreal, Canada). X-ray micro-CT images and Otsu segmented vugs of two of the samples are seen in Figures 2 and 3.

A set of eleven (11) carbonate samples consisting of a dielectric segment (6-8 mm thick) and a plug segment (~36 mm thick) were sliced from the scanned one-inch diameter plugs. These were cleaned and saturated with brines of various salinities in some, first by spontaneous imbibition, and in all by vacuum saturation. As brine saturations changed, sequential dielectric and NMR T_2 measurements were made on the thin samples. Multi-dimensional NMR measurements were made on the plug segments.

All plug samples were saturated with 10% sodium chloride brine prior to NMR testing. For the smaller dielectric samples, two separate sequences of saturation and measurement were employed.

In one group of samples, spontaneous imbibition steps identified by changes in the slope of weight increase with time were used to pull samples for concurrent dielectric and NMR T_2 measurements. A final saturation was achieved using cycles of vacuum and pressure. Salinity changes were made by soaking samples in successively higher sodium chloride concentrations for periods in excess of two weeks. The other group of samples were handled similarly but without the incremental imbibition steps.

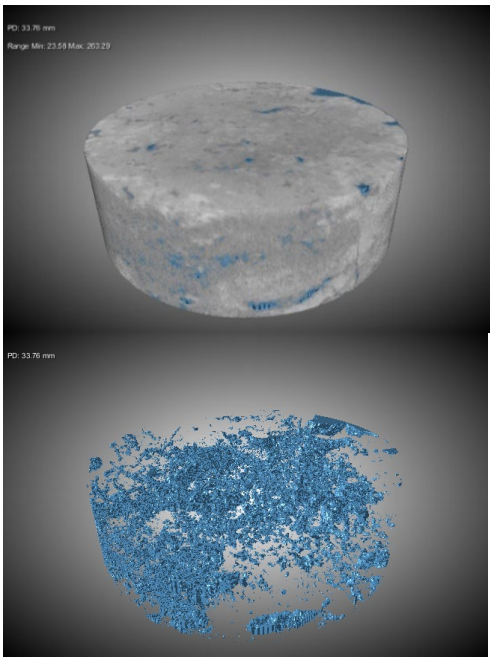

Figure 2 - Sample A4_D micro-CT image with Otsu threshold segmented vug fraction. Vug fraction is 4.27% of the bulk volume.

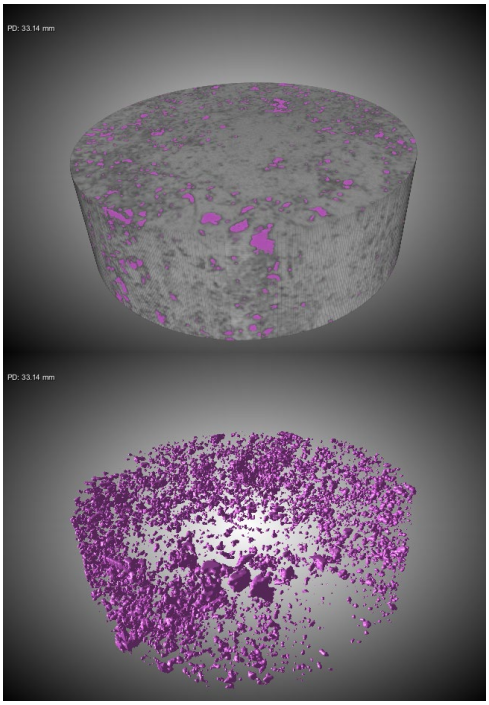

Figure 3 - Sample B1_D micro-CT image with Otsu threshold segmented vug fraction. Vug fraction is 1.48% of the bulk volume.

2.2 Dielectric Measurements

In the frequency range of 1 to 300 MHz, the most accurate technique for impedance measurements uses a calibrated capacitance cell. The cell is configured to minimize electrode potentials with gold plated contacts. Thin, brine saturated cellulose interfaces provide contact coupling with the samples. In our experiments, an HP 4291A impedance analyzer is in series with an HP 4289 bridge, an HP 4291B high impedance head test port, and a robust GenRad sample holder. The system communicates via an HPIB connection with a desktop workstation running National Instruments VISA software. The system is controlled and the recoded data is analyzed with a MATLAB acquisition and processing program.

Following an initial multi-step calibration of the HP 4291A and HP 4289 for open, short, load, and electrical length, the calibration is repeated at each sampling frequency with the sample holder in place. The measurement, commonly described as the RF-IV method, uses two sensitive high-speed voltmeters in the HP 4291A to measure the source voltage and the reflected current.

2.3 NMR Measurements

NMR measurements were made on Oxford Instruments (Maran Ultra) 2 MHz and an Oxford MQC 23 MHz system. The 2 MHz systems were equipped with 1D gradients enclosing a 50 mm diameter probe. Typical 90° pulse widths were 20 microseconds and CPMG echo spacings (2* tau) were 200 microseconds. The 23 MHz system used a 30mm probe with tau values from 30 to 1000 microseconds. Recycle delays for both systems ranged from 7.5 to 15 seconds depending on the sample. Standard CPMG and inversion recovery pulse sequences were used for the and T_1 / T_2 measurements.

NMR T_1/T_2 measurements were done on fully saturated and selected samples in both the 2 MHz and the 23 MHz systems. Pulse sequences followed the parameters used in the T_2 measurements for 30 T_1 tau values logarithmically spaced from 1 msec to 3 seconds.

3 Results and Discussion

3.1 Dielectric and NMR Distributions of Relaxation Times

Dielectric dispersion in carbonates scales with conductivity[23, 24] such that the normalized dielectric dispersion results shown in Figure 4 are consistent for all brine concentrations. The corresponding 23 MHz NMR T_2 distributions are shown in Figure 5.

In Figure 4 the lower dielectric constant values for samples A1_D and A2_D provide no direct information on the bi-modal nature of the pore system that is apparent in the NMR response shown in Figure 5. However, imbibition results do provide an indicator of NMR and dielectric associated responses. For sample B1_D there was no measurable change in saturations between the first imbibition and second imbibition cycles, However, there were slight changes in the dielectric dispersion curves in Figure 6 and the corresponding NMR T_2 distribution curves in Figure 7.

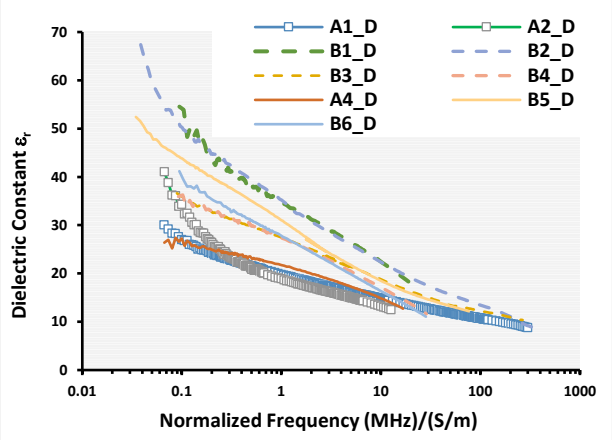

Figure 4 - Conductivity normalized dielectric constant dispersion for brine saturated Michigan carbonate samples.

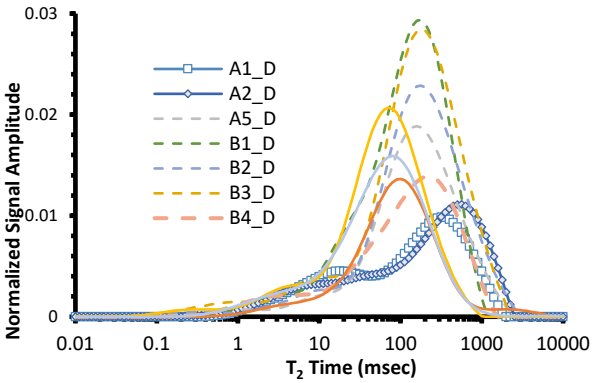

Figure 5 - 23 MHz Normalized NMR T_2 distributions for brine saturated Michigan carbonate samples.

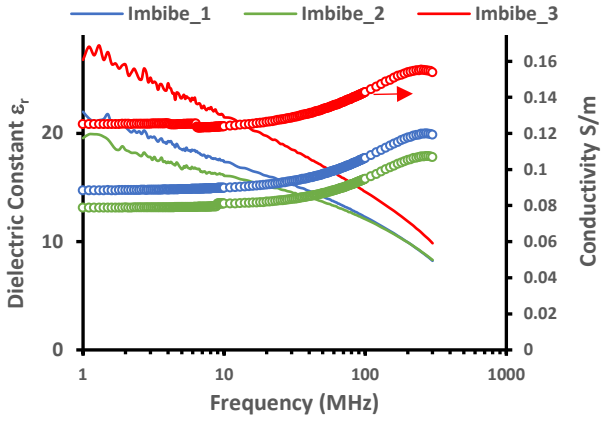

*Figure 6 -Sample B1_D imbibition stage ϕ*Sw dielectric dispersion data. Second imbibition step shows lower dielectric response between first and second imbibition.*

One inference from the NMR distributions is that the brine imbibed in the first cycle has re-distributed to slightly smaller pores by the end of the second cycle. As we shall see in our τ_{PCM} model this type of change would result in the slightly reduced dielectric dispersion results seen in the test.

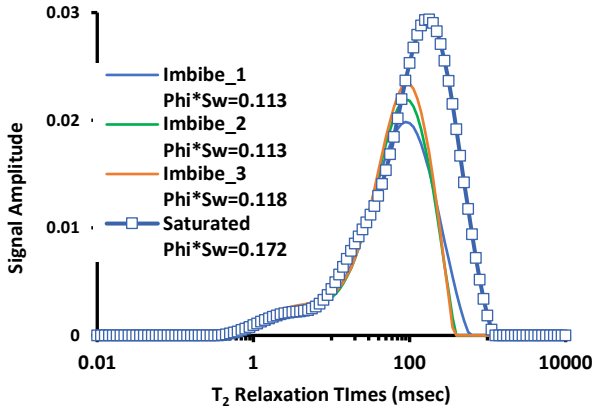

Figure 7 - Sample B1_D imbibition T_2 distributions showing shift to lower T2 times between the first and second imbibition cycles.

3.2 Dielectric and NMR Pore Combination Model (τ_{PCM})

The carbonate pore components that contribute to the overall dielectric response are illustrated in Figure 8. These components, identified by Myers [24] using thin-section discriminators for the vug and matrix components, have proven to be durable, physics-based combination.

Extending this concept to a more finely defined pore structure combination was an enticing opportunity. Frequency normalization of the measured dielectric response by conductivity of the brine focuses the model, eliminating salinity variability. A subsequent fit of the matrix and vug components to the HN equation, provides a rapid object function fit for the dispersion data. These fits for the real components of the dielectric constant for the matrix and vug components $\varepsilon_{r_{matrix}}$ and $\varepsilon_{r_{vugs}}$, are used to determine the matrix ϕ_{Agm}, and vug, ϕ_{Agv} porosity in the linear pore combination for ε_r where:

$$\varepsilon_r = \varepsilon_{r_{matrix}} \cdot \phi_{Agm} + \varepsilon_{r_{vugs}} \cdot \phi_{Agv} + \varepsilon_\infty \qquad (5)$$

The individual pore component dispersion curves are shown in Figure 8. The HN model values for τ in the two systems were: 1.93 e-10 sec. for the vug system and 5.47e-9 sec. for the matrix system. Using Equation (2) from the BPP model these give T_1 values of 101.5 msec and 3.6 msec for the vug and matrix systems respectively.

A linear fit of Equation (5) for the fully saturated frequency normalized dielectric response of Sample B3_D is shown in Figure 9.

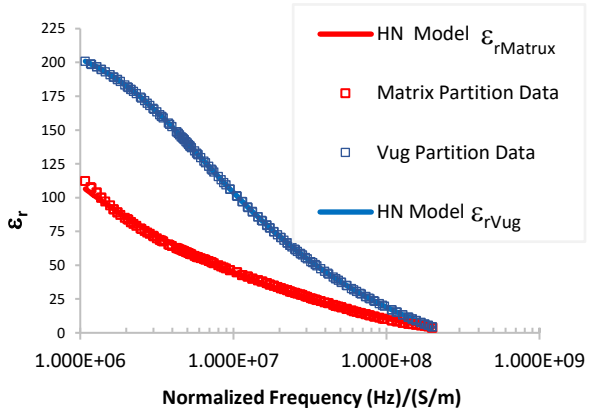

Figure 8 - Myers pore combination model matrix and vug dielectric dispersion curves with HN model fit.

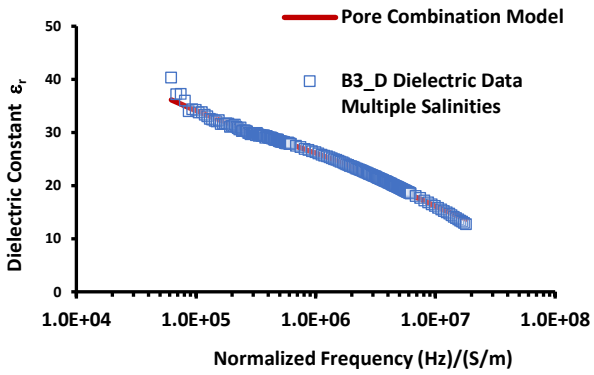

Figure 9 - Pore combination components and example fit using phi Vug= .065, phi matrix = .055, epsilon infinity= 6.862

The τ_{PCM} model essentially distributes the matrix fraction derived from the PCM fit onto the T_2 distribution. Attempts to use a simple T_2 cutoff failed to accurately capture a consistent size or size differential throughout the data set pointing to the need for a "spectral" distribution similar to that used for Swi evaluations in NMR data.

The proposed model assumes that the fractional matrix contribution to the dielectric intensity and dispersion starts first with the fastest relaxing NMR regions in the sample. It also assumes that the intensity of the interaction falls off with distance in a manner consistent with Debye shielding described in Equation (6).

$$\psi_V = \psi_S e^{-r/\lambda_D} \qquad (6)$$

Substituting incremental T_2 values for r and constraining the matrix response to the pore combination model matrix fraction (ϕ_{AGM}), the derived spectral distribution parameter is the best fit for τ_{PCM} based on Equation (7). T_2 signal amplitudes at each T_2 are then

linear combinations of M_{Agm} and M_{Agv} determined from Equations (8) and (9).

$$\frac{\phi_{Agm}}{\phi_T} = \sum_{i=n}^{i=1} \left[\frac{M(T_{2_i})}{M_T} \right] e^{-T_{2i}/\tau_{PCM}} \quad (7)$$

$$M_{Agm}(T_{2_i}) = M(T_{2_i}) e^{-T_{2i}/\tau_{PCM}} \quad (8)$$

$$M_{Agv}(T_{2_i}) = M(T_{2_i})(1 - e^{-T_{2i}/\tau_{PCM}}) \quad (9)$$

Comparative results showing the range of distributions and their variability in the dielectric data are seen in the two dielectric samples shown in Figure 10 with distributions highlighted in Figures 11 and 12.

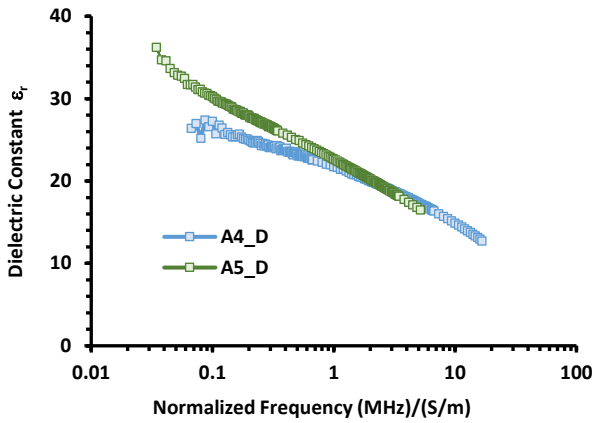

Figure 10 -Dielectric constant dispersion results for saturated samples A4_D and A5_D.

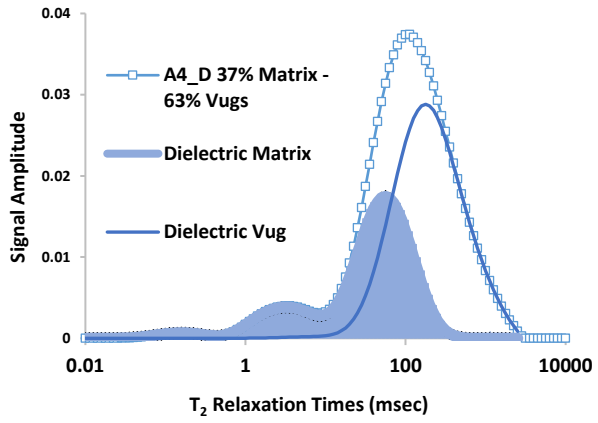

Figure 11 –T_2 mapped dielectric matrix and vug pore combinations for Sample A4_D. Matrix volume fraction 37%, Vug volume fraction 63%.

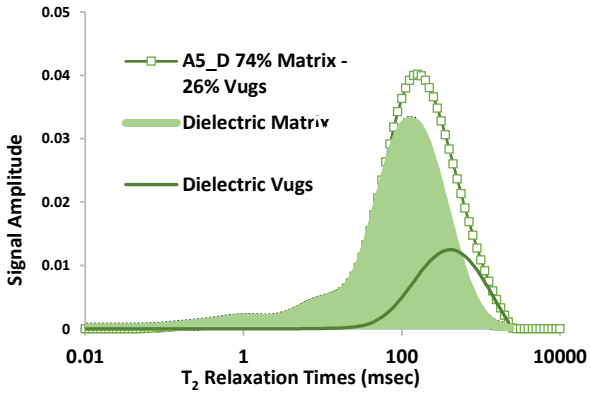

Figure 12 - T_2 mapped dielectric matrix and vug pore combinations for Sample A5_D. Matrix volume fraction 74%, Vug volume fraction 26%

T_2 mapped dielectric matrix and vug distributions for all samples are shown in Figures 13 and 14 and listed in Table 1.

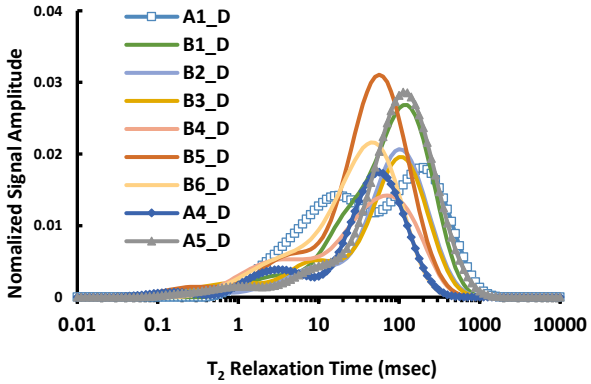

Figure 13 - Normalized T_2 mapped dielectric matrix components for brine saturated Michigan carbonate samples.

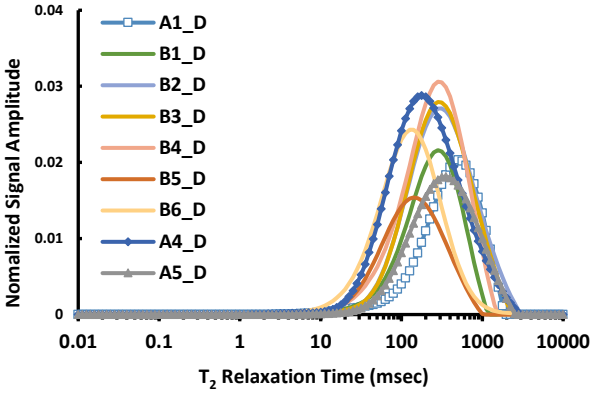

Figure 14 - Normalized T_2 mapped dielectric vug components for brine saturated Michigan carbonate samples.

Table 1 - Matrix and vug fractions determined from the normalized dielectric response and corresponding τ_{PCM}

Sample	τ_{PCM}	Fraction		
		Matrix	Vugs	Phi
A1_D	420	0.652	0.348	0.083
A4_D	96	0.370	0.630	0.081
A5_D	395	0.610	0.340	0.098
B1_D	315	0.638	0.362	0.172
B2	282	0.526	0.474	0.143
B3	190	0.455	0.545	0.13
B4_D	132	0.426	0.574	0.098
B5	221	0.703	0.297	0.119
B6_D	104.5	0.531	0.469	0.113

The mapping parameter for the dielectric matrix distributions, τ_{PCM}, was developed using exclusively the real component of the complex dielectric equation. The fundamental Kramer's–Kronig relationship states that there should also be a relationship with the complex part of the dielectric equation. In this case the conductivity. Figure 15 shows this relationship. Here the formation factor was calculated using the 10 MHz value for conductivity. The dielectric pore combination model works well but breaks down with samples that show a single vug connection that covers the width of the sample such as Sample A2_D, which is not included in the analysis.

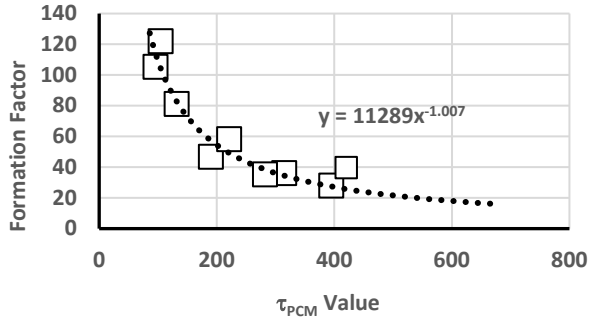

Figure 15 - Formation factor Correlation for τ_{PCM}

Tableau 2 - Sample Formation factor and corresponding Tau-PCM values

Sample	τ_{PCM}		FF	
		Phi	C_w/C_{10MHz}	m
A1_D	420	0.083	39.83	1.48
A4_D	96	0.081	105.24	1.85
A5_D	395	0.098	28.00	1.55
B1_D	315	0.172	36.16	2.04
B2_D	282	0.143	35.31	1.83
B3_D	190	0.13	46.65	1.88
B4_D	132	0.098	81.17	1.89
B5_D	221	0.119	58.25	1.91
B6_D	104.5	0.113	122.00	2.20

Spectral mapping of dielectric dispersion onto T_2 distributions provides a unique phenomenological model for linking two petrophysical tools and measurements. It shows clearly that "one size does not fit all" when defining a vug. The model supports the idea that the electromagnetic interactions are not size specific. It suggests that variations in the electric fields in a sample are related to the size of an inclusion and to the size of any surrounding inclusions. An ideal first step to validate the model and to establish theoretical support is to "look at the rocks".

4 Results

4.1 Imaging Carbonate Structure

Partitioning pore space using size and descriptive parameters is a fundamental practice in petrology and petrophysics. Introducing dielectric measurements to the mix is relatively new.

Early work in machine learning applied to thin sections and SEM backscattered images provides a qualitative tool to assess the duality in size related dielectric constants for the τ_{PCM} model.

Carbonate pore typing described by Ross [25] illustrates end-member characteristics that quantify the "rough" and "smooth" pore characteristics seen in SEM images. The areas are determined by erosion and dilation sequences associated with the number of size correlated cycles. Quantitative results are shown in Figure 16. The largest two end members listed are typical of the thin section and micro-CT porosities visible in this set of samples.

SEM Image	Rough Area		Smooth Area	
	Size	%	Size	%
	0-12	10	0-8	90
	0-12 12-23	50 8	0-8 8-31	19 23
	0-12 12-23 23-42	19 32 20	8-31 31-69	12 15
	12-23 23-42 42-76 76-210	2 19 38 10	31-69 69-134	4 20
	23-42 42-76 76-210	2 12 50	69-134 134-210	2 22

Figure 16 – SEM - Smooth and Rough areas based on erosion-dilation cycles. All sizes are in microns.

All sizes have some smooth and some rough areas. Overlaying the SEM sizes with the T_2 distributions puts smooth and rough areas in the 50 – 1200 msec T2 range.

where there exists both matrix and vug components in relative ratios similar to the rough to smooth ratios of the SEM.

4.2 Saturation Effects

In addition to describing the dielectric dispersion of the pore combinations, Figure 8 illustrates differences in the dielectric constant for matrix and vug components at the NMR frequencies of 2 and 23 MHz. At 2 MHz the vug/matrix dielectric factor is 2.07 and 2.34 at 23 MHz.

These differences suggest that any measured dielectric value is sensitive to the distribution of fluids between matrix and vugs. Even to the extent where spatial variation can override saturation changes. This was indeed the case as shown by the Imbibe_1 dielectric and NMR response compared to Imbibe_2 for Sample B1_D shown in Figures 6 and 7 and for Sample B6_D in Figures 17 and 18.

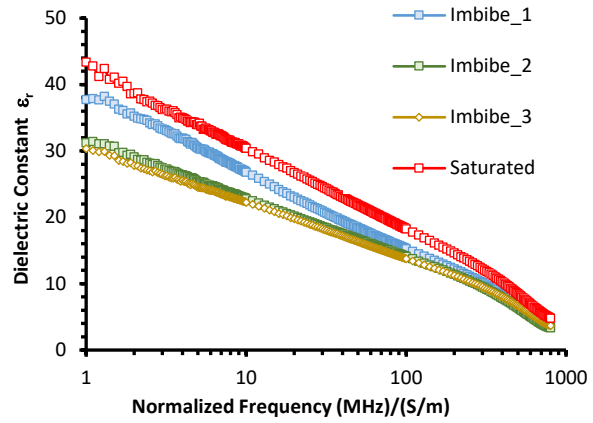

Figure 17 - Dielectric dispersion for imbibition cycles in Sample B6_D.

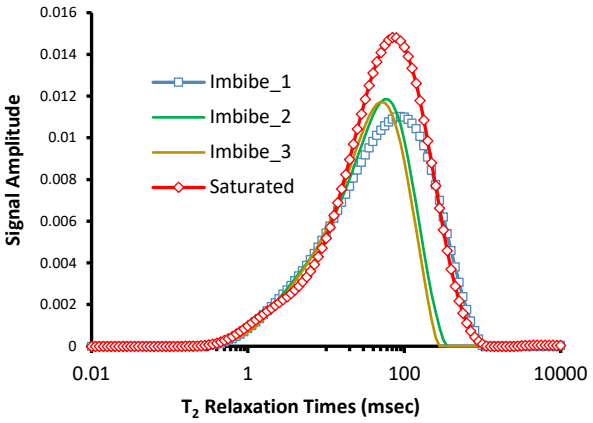

Figure 18 - Imbibition cycle NMR T_2 distributions for Sample B6_D.

The use of Equations (7) thru (9) and the correlation shown in Figure 15, was adapted based on samples with $\phi Sw = \phi$. Results for imbibition samples provided a convenient check on the model for lower values of ϕSw.

After partitioning the dielectric response for the partially saturated samples using matrix and vug dispersion functions shown in Figure 8, corresponding τ_{PCM} terms were determined and evaluated for their formation factor dependence. Values for four saturations established in sample B4_D are listed in Table 3. Higher saturations generally show better agreement due to the data density. Adding lower saturation values into the Figure 15 correlation should improve the model.

Table 3-Sample B4_D Imbibition Cycles-τ_{PCM} results

Imbibition			Formation Factor	
	Tau_Pcm	Phi*Sw	Experimental	Model
Imbibe_1	55.8	0.050	252	197
Imbibe_2	52.6	0.048	248	209
Imbibe_4	65.1	0.064	175	168
Saturated	132	0.098	81.2	79.6

5 Diffusion Correlations

The close connection of τ_{PCM} with the formation factor indicates that diffusion effects may be quantifiable with this technique. Based on ratios of restricted and unrestricted mean squared distance the equation,

$$\frac{D_{eff}}{D_0} = \frac{1}{FF \cdot \phi} \tag{10}$$

where D_{eff} is the effective diffusion, D_0 is the molecular self-diffusion, FF and phi are the formation factor and porosity, can be considered along with the equation relating the enhanced T_2 relaxation times at variable inter-echo times.

$$\frac{1}{T_{2D}} = \frac{1}{3}(\tau\gamma G)^2 D \tag{11}$$

In combination with the τ_{PCM} distributions, the variable tau technique can provide information on the relative diffusivity or internal gradients (G) in both the matrix and vug systems. Just as plots of the log mean T_2 values versus tau can be used for the entire sample, shifts for the matrix and vug distributions can provide comparative results for the effective diffusion in the two systems or for estimates of their internal gradients. An example of different shifts (matrix versus vug) for one of the samples is shown in Figures 19. Agreement between the sample and the dielectric determined formation factor is shown in Figure 20. The best agreement between the techniques used sample T_{2D} values with G_{Sample}=68.1 Gauss/cm or G_{Vug}=67.8 Gauss/cm and G_{Matrix}=120 Gauss/cm.

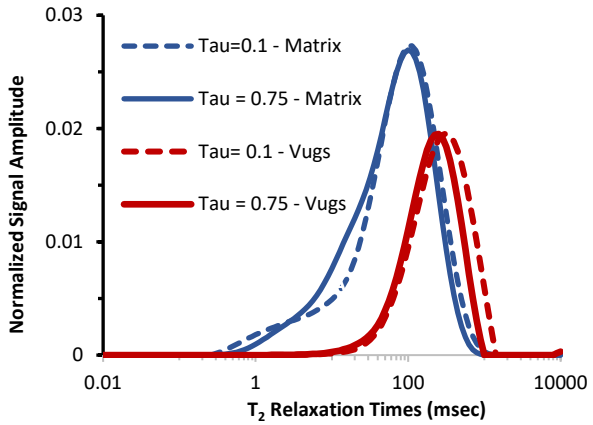

Figure 19 - Tau-pcm distributions with variable inter-echo spacing for Sample B1_D with. D_{eff}=4.18 e-10 m2/sec

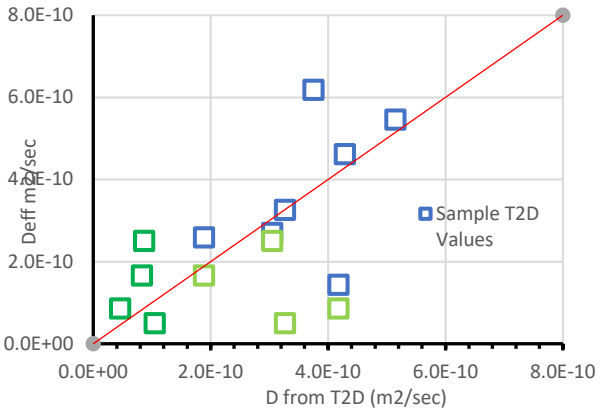

Figure 20 - Diffusion coefficients determined for dielectric from formation factor and variable tau measurements. Optimized with G determined as 68.1 Gauss/cm or Sample T2D.

5.1 T_1/T_2 Variations

Initial comparisons of 2 MHz and 23 MHz T_1/T_2 plots shown in Figure 21 and Figure 22 indicated that greater separation of relaxation mechanisms predicted by the BPP model (Figure 1) may be accessible.

Comparisons of Figure 22 with Figure 23 show the development of a secondary, horizontally developed, T_2 independent peak at long T_1 times. This peak is pronounced in Sample B4_D but develops in other samples as the vug fraction increases. The plots highlight different matrix fractions and relative differences in the build-up of the vug component in Samples B2_D and B4_D.

T_1/T_2 response differences would not be predicted simply by comparison of the T_1 or T_2 distributions. However, the application of the mapped dielectric partitioning (Figures 24 and 25) highlights the vug T_2 differences that are distinct and identifiable in long relaxing T_1 components (Figures 21 and 22).

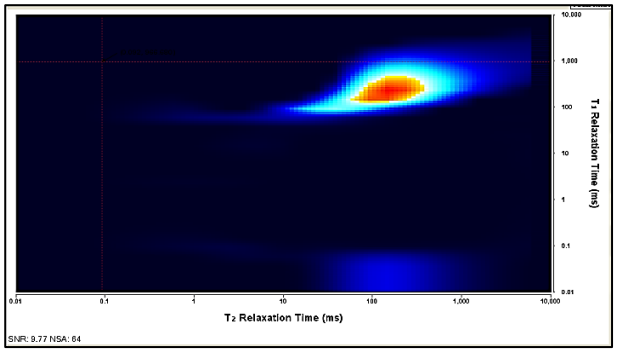

Figure 21 - 2 MHz T_1/T_2 plot for Saturated sample B2_D. As expected from BPP model there is less separation in the T_1 and T_2 peaks.

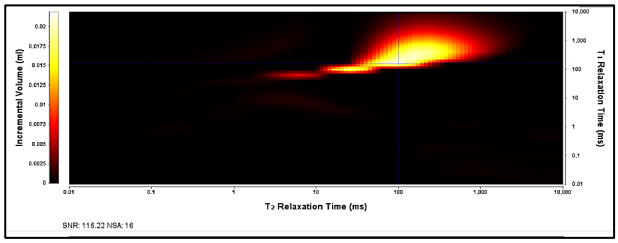

Figure 22 - T_1/T_2 plots at 2 MHz and 23 MHz for Sample B2_D. Better separation of the T_2 and T_1 elements reflects the T_1 and T_2 vertical separation seen in BPP model .

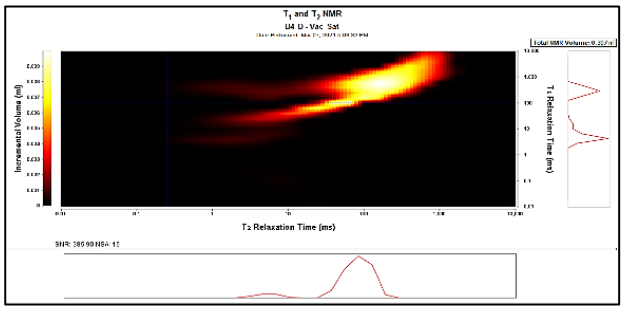

Figure 23 - T_1/T_2 plot for Sample B4_D, (Matrix Fraction = .426) showing the development of T_2 independent peak in the vug partition.

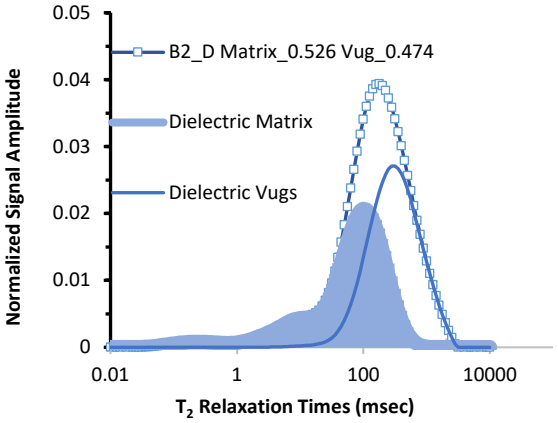

Figure 24-Partitioning of dielectric matrix and vug components for Sample B2_D under the normalized T_2 distribution.

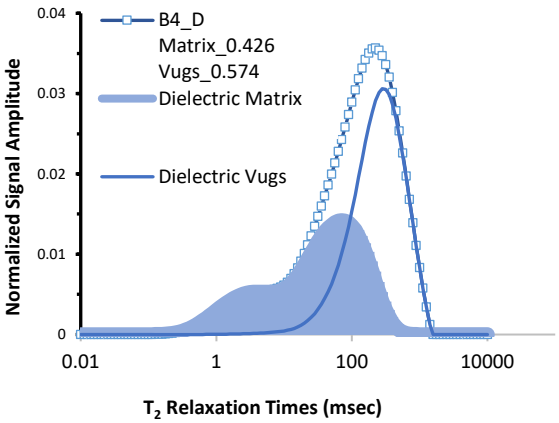

Figure 25 - Partitioning of dielectric matrix and vug components for Sample B4 under the normalized T_2 distribution.

6 Discussion

Dielectric analyses that follow the ideas of Maxwell-Garnet model focus on defining the electric field in an assortment of pore space geometries that incorporate geometrical orientation in the field. Although successful in practice a viable alternative is to use a fundamental measurement that reflects the geometry of the pore space. NMR T_2 distributions provide that information in an integral form. Our τ_{PCM} model allows us to differentiate the integral with respect to the dielectric constant and quantify the relative geometrical contributions of the matrix and the "vug" system.

Pore space imaging and specific petrophysical measurements for formation factor, resistivity index, and restricted diffusion provide validation and quantification for the differential mapping of dielectric responses to the T_2 spectrum. NMR T_1/T_2 dimensional measurements provide additional information that elucidate possible selective relaxation mechanisms for the different geometrical contributors.

The good agreement of saturation dependence with τ_{PCM} supports the linear relationship established by the technique and the established linear relationship between vug porosity and formation factor inherent in the pore combination model. It suggests that τ_{PCM} provides a modeled saturation discriminator for the matrix and vug systems more easily applied than the geometric terms used in the derivation of water tortuosity.

7 Conclusions

Spectral mapping of the dielectric response onto the NMR T_2 distributions provides a quantitative petrophysical tool useful for pore space characterization and saturation mapping. The model provides a dielectric description of the T_2 relaxation spectrum constrained by the surface to volume correlations of the Brownstein and Tarr model.

The ability to distinguish the matrix and vug contributions in a system dominated by surface relaxivity (fast diffusion limit) is an essential step, comparable to that seen with D_2O displacement studies, to characterizing bi-modal fluid transport in conventional carbonates.

The utility of our τ_{PCM} application to the magnetization components of the T_2 distribution indicates that location characteristics of the dielectric constant are captured in our normal pulse sequences applied during a CPMG experiment.

The comparisons and agreements with previous and current work confirm the applicability of the technique and suggest that a progression beyond that of a phenomenological model is warranted.

8 Nomenclature

Physical Constants

τ_c – *Autocorrelation time* (*nanoseconds*)

$\hbar$ – *Planck's constant* $1.05457\times10^{-34}(J\cdot s)$

μ_0 – *Permeability of free space* $1.256637\times10^{-6}(H/m)$

ω_0 – *NMR resonant frequency* (*radians / sec*)

γ – *Proton gyromagnetic ratio* 267.515×10^{-6} $(rad/s\cdot T)$

ψ_V – *Electric potential* (*microvolts*)

ψ_S – *Surface potential* (*microvolts*)

λ_D – *Potential shielding distance* (*nanometers*)

Dielectric Terms

ε^* – *Complex relative permitivity*

ε_∞ – *high frequency relative permitivity limit*

ε_s – *low frequency relative permitivity*

ε_r – *Real component of the complex relative permitivity*

ω – *frequency for dielectric dispersion*

τ_{PCM} – *Dieletric to NMR mapping constant* (*microseconds*)

ϕ_{Agm} – *Porosity of the matrix component*

ϕ_{Agv} – *Porosity of the vug component*

NMR Terms

$T_1 - Spin - lattice\ relaxation\ time\ (msec)$

$T_2 - Spin - Spin\ relaxation\ time\ (msec)$

$T_{2D} - Relaxation\ time\ due\ to\ diffusion\ (msec)$

$M\left(T_{2i}\right) - Signal\ amplitude\ (magnetization)\ at\ T_2\ time$

$D_{eff} - Effective\ diffusion\ coefficient\ (m^2/sec)$

$D_0 - Liquid\ diffusion\ coefficient\ (m^2/sec)$

$G - Magnetic\ gradient\ strength\ (Gauss/cm)$

$\tau - CPMG\ interecho\ spacing\ (msec)$

9 Bibliography

[1] N. Bloembergen, E.M. Purcell, R.V. Pound, Relaxation effects in nuclear magnetic resonance absorption, Physical Review 73(7) (1948) 679-712.

[2] K. Kabara, V. Madhurima, A.C. Kumbharkhane, A.V. Sarode, Study of H1 spin lattice relaxation and dielectric relaxation in Poly(propylene glycol) system, Materials Chemistry and Physics 209 (2018) 16-22.

[3] M. Fukuzaki, N. Miura, N. Shinyashiki, D. Kurita, S. Shioya, M. Haida, S. Mashimo, Comparison of water relaxation time in serum albumin solution using nuclear magnetic resonance and time domain reflectometry, Journal of Physical Chemistry® 99(1) (1995) 431-435.

[4] D. Kruk, E. Masiewicz, M. Wojciechowski, M. Florek-Wojciechowska, L.M. Broche, D.J. Lurie, Slow dynamics of solid proteins - Nuclear magnetic resonance relaxometry versus dielectric spectroscopy, J Magn Reson 314 (2020) 106721.

[5] S. Godefroy, J.P. Korb, M. Fleury, R.G. Bryant, Surface nuclear magnetic relaxation and dynamics of water and oil in macroporous media, Phys Rev E Stat Nonlin Soft Matter Phys 64(2 Pt 1) (2001) 021605.

[6] E. Müller-Huber, F. Börner, J.H. Börner, D. Kulke, Combined interpretation of NMR, MICP, and SIP measurements on mud-dominated and grain-dominated carbonate rocks, Journal of Applied Geophysics 159 (2018) 228-240.

[7] Z. Zhang, S. Kruschwitz, A. Weller, M. Halisch, Enhanced pore space analysis by use of μ-CT, MIP, NMR, and SIP, Solid Earth 9(6) (2018) 1225-1238.

[8] E. Toumelin, C. Torres-Verdin, N. Bona, Improving Petrophysical Interpretation With Wide-Band Electromagnetic Measurements, SPE Journal 13(02) (2008) 205-215.

[9] E. Toumelin, Pore-scale petrophysical models for the simulation and combined interpretation of nuclear magnetic resonance and wide -band electromagnetic measurements of saturated rocks, ProQuest Dissertations Publishing, 2006.

[10] F. C. Ferreira, M. Stukan, L. Liang, A. Souza, L. Venkataramanan, A. Beletskaya, D. Dias, M. Dantas da Silva, New Model for Wettability Change with Depth in Mixed-Wet Complex Carbonates, Abu Dhabi International Petroleum Exhibition & Conference, Society of Petroleum Engineers, Abu Dhabi, UAE, 2018, p. 28.

[11] B. Sauerer, A. Valori, D. Krinis, W. Abdallah, NMR Wettability of Carbonate Reservoir Cores: Best Practices, SPE Middle East Oil and Gas Show and Conference, Society of Petroleum Engineers, Manama, Bahrain, 2019, p. 17.

[12] Y. Marcus, Effect of Ions on the Structure of Water: Structure Making and Breaking, Chemical reviews 109(3) (2009) 1346-1370.

[13] E. Levy, A. Puzenko, U. Kaatze, P.B. Ishai, Y. Feldman, Dielectric spectra broadening as the signature of dipole-matrix interaction. II. Water in ionic solutions, The Journal of chemical physics 136(11) (2012) 114503-114503-6.

[14] P.T. Callaghan, Translational Dynamics and Magnetic Resonance: Principles of Pulsed Gradient Spin Echo NMR, OUP Oxford2011.

[15] C.P. Poole, H.A. Farach, CHAPTER 20 - Dielectric Relaxation, in: C.P. Poole, H.A. Farach (Eds.), Relaxation in Magnetic Resonance, Academic Press1971, pp. 319-350.

[16] J.P. Poley, J.J. Nooteboom, P.J. De Waal, Use Of V.h.f Dielectric Measurements For Borehole Formation Analysis, SPWLA-1986-vXXVIIn1a4 19(03) (1978) 35.

[17] M. Sliwinska-Bartkowiak, J. Gras, R. Sikorski, R. Radhakrishnan, L. Gelb, K.E. Gubbins, Phase Transitions in Pores: Experimental and Simulation Studies of Melting and Freezing, Langmuir 15(18) (1999) 6060-6069.

[18] W.T. Coffey, Dielectric relaxation: an overview, Journal of Molecular Liquids 114(1) (2004) 5-25.

[19] Y. Feldman, A. Puzenko, P. Ben Ishai, A. Gutina Greenbaum, The dielectric response of interfacial water—from the ordered structures to the single hydrated shell, Colloid and Polymer Science 292(8) (2014) 1923-1932.

[20] N. Cassidy, Electrical and magnetic properties of rocks, soils and fluids, Ground Penetrating Radar2009, pp. 41-72.

[21] T.L. Chelidze, Y. Gueguen, Electrical spectroscopy of porous rocks: a review—I.Theoretical models, Geophysical Journal International 137(1) (1999) 1-15.

[22] S. Havriliak, S. Negami, A complex plane representation of dielectric and mechanical relaxation processes in some polymers, Polymer 8 (1967) 161-210.

[23] W.E. Kenyon, Texture effects on megahertz dielectric properties of calcite rock samples, Journal of Applied Physics 55(8) (1984) 3153-3159.

[24] M.T. Myers, Pore Combination Modeling: A Technique for Modeling the Permeability and Resistivity Properties of Complex Pore Systems, SPE Annual Technical Conference and Exhibition, Society of Petroleum Engineers, Dallas, Texas, 1991, p. 11.

[25] C.M. Ross, C.A. Callender, J.B. Turbeville, J.J. Funk, Modeling of Capillary Pressure Behavior Using Standard Open Hole Wireline Log Data: Demonstrated on Carbonates from the Middle East, SPE Annual Technical Conference and Exhibition, Society of Petroleum Engineers, Dallas, Texas, 1995, p. 12.